ERDC/CRREL TR-19-1

US Army Corps
of Engineers®
Engineer Research and
Development Center

ERDC
ENGINEER RESEARCH & DEVELOPMENT CENTER

Engineering for Polar Operations, Logistics, and Research (EPOLAR)

Microstructural Characterization of Snow Compaction Related to Snow Pavements

Zoe R. Courville, Ross M. Lieblappen, Terry D. Melendy, and Andrew P. Bernier

January 2019

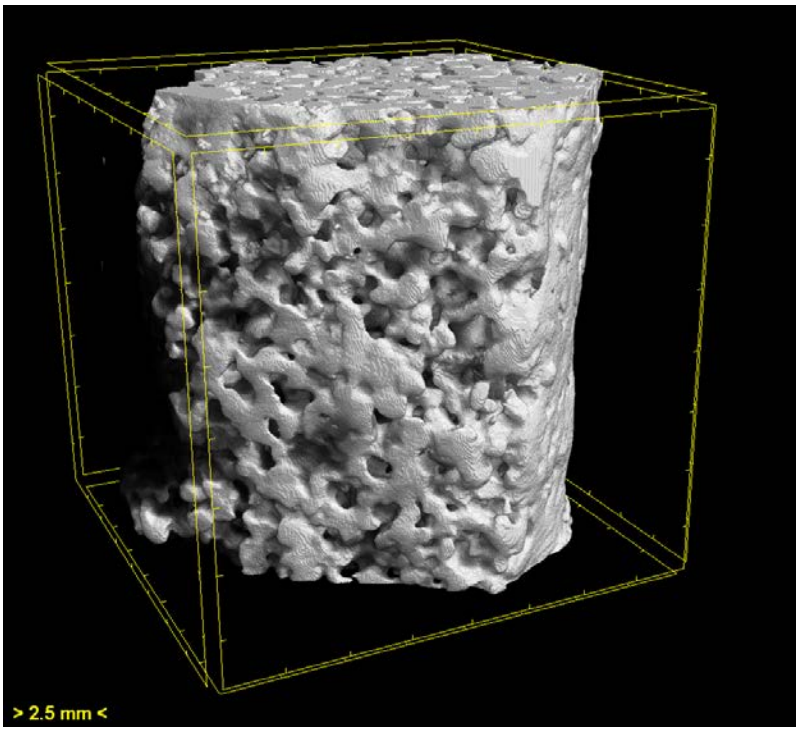

Cold Regions Research
and Engineering Laboratory

The U.S. Army Engineer Research and Development Center (ERDC) solves the nation's toughest engineering and environmental challenges. ERDC develops innovative solutions in civil and military engineering, geospatial sciences, water resources, and environmental sciences for the Army, the Department of Defense, civilian agencies, and our nation's public good. Find out more at www.erdc.usace.army.mil.

To search for other technical reports published by ERDC, visit the ERDC online library at http://acwc.sdp.sirsi.net/client/default.

Engineering for Polar Operations, Logistics,
and Research (EPOLAR)

ERDC/CRREL TR-19-1
January 2019

Microstructural Characterization of Snow Compaction Related to Snow Pavements

Zoe R. Courville, Ross M. Lieblappen, Terry D. Melendy, and Andrew P. Bernier

U.S. Army Engineer Research and Development Center (ERDC)
Cold Regions Research and Engineering Laboratory (CRREL)
72 Lyme Road
Hanover, NH 03755-1290

Final Report

Prepared for National Science Foundation, Office of Polar Programs
2415 Eisenhower Avenue
Alexandria, VA 22314

Under Engineering for Polar Operations, Logistics, and Research (EPOLAR)
EP-ANT-16-34, “Evolution of the Strength of Compacted Snow”

Abstract

A first-of-its-kind snow runway for wheeled aircraft operation at McMurdo Station, Antarctica, demonstrated that robust structures can be made of snow that push the limit of what is known about snow strength and how to parameterize it. We conducted a series of laboratory tests to determine the links between snow density and snow compressive strength for very high-density snow structures. We constructed snow samples of varying densities to mimic the snow structures of the constructed runway and measured the resulting snow microstructural and mechanical properties. The goal of this work is to ultimately increase our understanding of the role of density, as an easy-to-measure parameter, in determining snow strength as it relates to snow construction applications (e.g., snow runways, tunnels, and foundations) and how to best quantify the relationships between microstructure, density, and strength of very dense snow structures. Our values for the mechanical properties compared relatively well with the compilation of past historical results. Based on our results, to a first order approximation, snow microstructure data can be used to help improve snow strength predictions. Important future work would focus on improving these snow microstructure-strength relationships to include the effects of meteorological forcing.

Contents

Figures and Tables

Figures

Tables

Preface

This study was conducted for National Science Foundation (NSF), Office of Polar Programs, under Engineering for Polar Operations, Logistics, and Research (EPOLAR) EP-ANT-16-34, "Evolution of the Strength of Compacted Snow." The technical monitor was Ms. Margaret Knuth, Operations Manager, NSF Antarctic Infrastructure and Logistics.

The work was performed by the Terrestrial and Cryospheric Sciences Branch (CEERD-RRG), the Force Projection and Sustainment Branch (CEERD-RRH), and the Engineering Resources Branch (CEERD-RRE) of the Research and Engineering Division (CEERD-RR), U.S. Army Engineer Research and Development Center, Cold Regions Research and Engineering Laboratory (ERDC-CRREL). At the time of publication, Dr. John Weatherly was Chief, CEERD-RRG; Dr. Harley Cudney was Acting Chief, CEERD-RRH; Mr. Jared Oren was Chief, CEERD-RRD; Mr. J. D. Horne was Chief, CEERD-RR; and Dr. Rosa Affleck was the program manager for EPOLAR. The Deputy Director of ERDC-CRREL was Dr. David Ringelberg, and the Director was Dr. Joseph L. Corriveau.

COL Ivan P. Beckman was Commander of ERDC, and Dr. David W. Pittman was the Director.

Acronyms and Abbreviations

CRREL	U.S. Army Cold Regions Research and Engineering Laboratory
EPOLAR	Engineering for Polar Operations, Logistics, and Research
ERDC	Engineer Research and Development Center
micro-CT	Micro-Computed Tomography
MTS	Materials Testing System
NSF	National Science Foundation
REV	Representative Elementary Volume
SSA	Specific Surface Area
S/V	Surface to Volume
2-D	Two-Dimensional
3-D	Three-Dimensional
UCS	Uniaxial Compressive Strength
USAF	U.S. Air Force
USAP	United States Antarctic Program

1 Introduction

1.1 Background

Recent U.S. Army Engineer Research and Development Center, Cold Regions Research and Engineering Laboratory (ERDC-CRREL), engineering efforts to develop a first-of-its-kind snow runway for wheeled aircraft operation at McMurdo Station, Antarctica, have demonstrated that robust structures can be made of snow. These efforts have resulted in a snow-based pavement material that pushes the limits of what is known about snow strength and its parameterization.

1.2 Objectives

The main objective for this work is to determine the microstructural parameters, calculated from micro-computed tomography (micro-CT) data analysis, that best predict corresponding snow strength. The broader goal of this work is to better understand the role of density, as an easy-to-measure parameter, in determining snow strength as related to using snow as a construction material (e.g., snow runways, tunnels, and foundations) and how to best quantify the relationships between microstructure, density, and strength for very dense snow structures. Though outside the scope of this report, important future work would focus on improving the predictions of snow strength, including the effects of meteorological forcing

1.3 Approach

We conducted a series of laboratory tests to determine the links between snow density and microstructure and snow compressive strength for very high-density snow structures. In the laboratory, we constructed a series of snow samples to mimic the snow structures of the Phoenix Runway, measured the resulting snow microstructural and mechanical properties, and compared these measurements to naturally occurring compacted firn samples of similar density. We determined three-dimensional (3-D) snow microstructural characteristics from micro-CT scans of the samples and determined snow strength from large-scale and small-scale compression tests and unconfined compressive-strength tests.

1.4 Prior Work

1.4.1 Snow runway development

In 2015, the United States Antarctic Program (USAP) began constructing a snow runway, now named the Phoenix Runway, to support wheeled flights on the McMurdo Ice Shelf 5 km east of the previously operated Pegasus Runway. The need for a new runway site arose from difficulties maintaining the Pegasus Runway, which was located in an ablation area and frequently experienced problematic dust deposition events that led to significant degradation due to melt. While skied aircraft landings on snow are relatively common, there are very few instances of building and operating deep-snow runways for wheeled aircraft. The Soviets operated a snow runway at Molodezhnaya, Antarctica, for ten years from 1981 to 1991 (Aver'yanov et al. 1983; Mellor 1993; Russell-Head and Budd 1989). The Australian Antarctic Division began constructing a compressed snow runway in Antarctica near Casey Station in the late 1980s but had to abandon this effort after conditions proved unfavorable for sustained operations (Russell-Head and Budd 1989). In general, there are two processes that must be performed to construct high-density snow, the first being compaction of the snow grains and the second entailing sintering of the snow, which is achieved by allowing processed snow surfaces to "rest" or "heal" and the bonds between grains to develop.

CRREL researchers designed the Phoenix deep-snow runway was designed to support flight operations for a U.S. Air Force (USAF) C-17 with a maximum gross weight of 227,000 kg Guidance for the construction and necessary snow strength requirements for aircraft operations on the runway is based on work by Abele (1968, 1990) and Moser and Sherwood (1968) and has been informed through a series of CRREL-lead construction and evaluation efforts prior to the certification of the runway (Haehnel et al. 2013, 2014). Table 1 presents the general design of the runway.

The runway was constructed in 7.5 cm lifts of compacted snow made by bulldozing snow onto the runway site from the surrounding natural snowpack. Measurements taken during January 2015 of the undisturbed, natural snow before the construction activities showed that the average density from the surface to a depth of 1 m at the Phoenix site was 480 kg/m^3. The average density was 400 kg/m^3 at the snow surface and 490 kg/m^3 at a depth of 1 m. Currently, USAP personnel monitor the density of the snow once a month at six locations along the length of the runway. The average

density of the surface postconstruction as of February 2016 for the base layer and the first lift (i.e., the bottom-most constructed level) was 630 kg/m^3, nearly 10% higher than the targeted design density of 575 kg/m^3. Table 2 presents the average snow densities of the natural, designed, and constructed runway over time.

Table 1. Runway cross sections as designed prior to construction. The density of the subgrade is determined from measurements made on natural, undisturbed snow in January 2015 prior to runway construction.*

Lift	Phoenix Target Lift Thickness (cm)	Depth to Bottom of Layer (cm)	Target Density (kg/m^3)	E_s (MPa)[K]	E_c (MPa)[B]	E_x (MPa)[E]	Unconfined Compressive Strength[A]	
							(psi)	(MPa)
5	7.5	7.5	675		1900	3000	363	2.5
4	7.5	15	675		1900	3000	363	2.5
3	7.5	23	650		1700	2700	290	2
2	7.5	30.5	600		1000	2100	203	1.4
1	7.5	38	575		600	2000	145	1
Base	7.5	46	525	100	360	1800	87	0.6
Subgrade			490					

[K] E_s = Static elastic modulus (data set K in Shapiro et al. 1997, Figure 6)

[B] E_c = Elastic modulus determined from uniaxial compression data (Shapiro et al. 1997, Figure 6); strain rate approximately 3×10^{-3} to 2×10^{-2} s^{-1} at −25 °C

[E] E_x = Complex modulus (Shapiro et al. 1997, Figure 6) evaluated at 103 Hz and −14 °C

[A] Abele (1990), most conservative estimate

* Table modified from Haehnel, R. B., G. L. Blaisdell, T. Melendy, S. Shoop, and Z. Courville, A Snow Runway for Supporting Wheeled Aircraft: Phoenix Airfield, McMurdo, Antarctica (forthcoming ERDC/CRREL TR), Hanover, NH, U.S. Army Engineer Research and Development Center.

Table 2. Phoenix Runway designed and as-constructed lift densities.*

Designed and Constructed Densities	Density (kg/m^3)	Standard Deviation (kg/m^3)
Natural Snow Base, at surface	400	
Natural Snow Base, at 1 m depth	490	
Natural Snow Base, average top 1 m	480	
Designed Lift Density	575	
Constructed Lift Density, February 2016, average top 1 m	580	30
Constructed Lift Density, December 2018, average top 1 m	638	47

* Table modified from Haehnel, R. B., G. L. Blaisdell, T. Melendy, S. Shoop, and Z. Courville, A Snow Runway for Supporting Wheeled Aircraft: Phoenix Airfield, McMurdo, Antarctica (forthcoming ERDC/CRREL TR), Hanover, NH, U.S. Army Engineer Research and Development Center.

The density of the top 10 cm layer of the runway varies considerably over the course of the year due to the construction schedule and to natural seasonal events (e.g., new snow accumulation and temperature fluctuations). For operational purposes, the density of the top 1 m of the runway is measured monthly at six sampling locations distributed along the length of the runway on the centerline. During the runway's first operational season, the density determined from approximately 1 m core measurements taken at the six sampling locations on 21 January 17 and measured using gravimetric methods (i.e., mass and volume measurements from cores) was 642 kg/m^3 with a standard deviation of 55 kg/m^3. For comparison, typical error associated with density determined from gravimetric means is within 10%–15% (or an error of about 65–100 kg/m^3 for snow from the runway). As construction and operations have continued on the runway, the average density of the top 1 m has approached values of 700 kg/m^3.

1.4.2 Snow strength as a function of snow structure

The most recent reviews of snow strength parameterizations are limited to densities less than 500 kg/m^3 (Petrovich 2003), with most snow mechanical studies focused on natural snow packs with even lower densities (Van Herwijnen 2016; Gerling 2017) In comparison, the average density of the top 1 m of the snow at the Phoenix Runway was approximately 700 kg/m^3 during construction and certification testing (Haehnel et al. 2018). Historically, research into snow mechanics has focused primarily on lower densities and strain rates approaching natural conditions, as reviewed by Shapiro et al. (1997), with limited direct property measurements for higher-density, artificially compacted snow.

Snow strength is ultimately determined by the microstructural properties of the snowpack. Snow grains sinter to form stress-concentrating bonds that range in diameter from 10 to 1000 µm. These bonds, or "necks," tend to concentrate stress because of their reduced cross-sectional area and highly curved surfaces (Salm 1982; Hagenmuller et al. 2014). These bonds are more likely to fail than other structural elements within the snow microstructure. It is only in recent years that full 3-D snow microstructure information has become available, thanks to the development of new imaging techniques. Laboratory tests have provided some limited direct mechanical observations of microstructural behavior related to snow strength (Reiweger and Schweizer 2010). These studies have focused primarily on densities of natural snowpacks for the purpose of assessing snowpack stability for avalanche forecasting.

2 Laboratory Methods

2.1 Snow-sample preparation

We tested artificially compacted snow and naturally compacted firn (polar snow) of varying densities by using two different compression stages. In the laboratory, we prepared snow specimens of uniform grain size of approximately 0.75 mm from sieved natural dry snow (using a mesh size of 0.5 to 1 mm diameter), which was then compacted and allowed to sinter to mimic a range of densities created on the Phoenix Runway. Samples were prepared in uniform cylindrical molds 5 cm in diameter and 15 cm in length. To mimic the runway construction process, we created the samples in "lifts" that were 1 to 5 cm thick by pouring loose, sieved snow into the molds and compacting using a heavy press and rubber mallet.

In the first round of testing, we made nine samples in 3–5 lifts, each 3–5 cm thick with an average density of 430 kg/m^3 ±15 kg/m^3. In the second round of testing, we used 8–10 lifts each 1–2 cm thickness to create an additional nine samples of denser snow (average 570 kg/m^3 ±13 kg/m^3 determined from weighing and measuring the core geometry). The resulting samples were placed in a −25°C cold room for 24 hours to allow the snow grains to sinter and to mimic runway snow construction techniques. The cores were then cut and the ends were leveled so that each core was 15 cm long. To replicate the snow pavement surface at the Phoenix runway, our target density for our laboratory samples was 700 kg/m^3. Using our laboratory sieving and compaction methods, the highest-density snow that we were able to create was 590 kg/m^3; the density of the prepared samples was limited ultimately by the fracture and failure of the samples as we prepared them through compaction. To examine the impact of varying microstructural geometry on snow strength, we also tested natural firn samples from a 20 m depth from an Arctic high-latitude ice sheet site with similar densities to the samples we created in the lab. These samples had similar densities, but very different microstructural characteristics.

To ensure that we tested representative volumes of the snow materials, we also examined larger samples that we constructed by sieving and compacting into a 30 cm by 25 cm rectangular mold. For the purpose of in situ compression tests within the micro-CT chamber, we cut smaller subsamples (1 cm diameter by 1.5 cm) from the larger (5 cm diameter by 15 cm) samples.

2.2 Microstructural characterization

We characterized snow microstructure by using a micro-CT scanner (a Bruker SkyScan 1173) housed in a cold room at −10°C. Micro-CT scans of the parent material were taken before and after compression testing. Microstructural characteristics, including snow specific surface area (SSA), grain size, porosity, grain connectivity, anisotropy, and density were computed from the 3-D micro-CT image data using the software program CT-Analyzer by Bruker. Snow SSA is related to the optical snow grain size, D_0, where $D_o = 6/\mathrm{SSA}$, and is a parameter used widely throughout snow science as a quantitative measurement of snow microstructure. Image processing included smoothing the raw x-ray data to reduce noise; reducing effects from beam hardening and thermal shifts that occur during the scan; postalignment of the data in relation to pre- and postreference scans; and removing image artifacts, including rings from dead pixels in the x-ray detector. . To segment the grayscale images into black (air) and white (ice) phases, we determined a global threshold by averaging the grayscale histograms of each individual two-dimensional (2-D) slice of the reconstructed micro-CT data set and choosing the local minimum between the two peaks, signifying the individual phases. Values below this threshold value were assigned to the air phase, and values above this threshold were assigned to the ice phase. Values of density determined from the micro-CT data value differ from the density determined via gravimetric methods by 1% to 20%, depending on the sample type. The values of the thresholded density data from the naturally compacted firn with large ice-grain sizes are generally within 1%–2% of gravimetrically determined density values while the artificially compacted snow samples with smaller ice grains have larger errors in the thresholded data (10%–20%). The dependency of the density values determined from the binarized micro-CT data on grain size is due to the influence of mixed pixels and difficulties resolving smaller grains at midresolutions.

Using the microstructural data, we identified the area within the 3-D micro-CT data that represented the smallest connection surface between any two sections of the snow sample by using the maximum-flow/minimum-cut (max-flow/min-cut) method based on network theory analysis (Hagenmuller et al. 2014). This method is primarily used to examine other porous media (e.g., bone and in medical applications [Tabor 2007]). The method we developed treats the ice phase as a collection of nodes, with one node at each voxel classified as ice. If two neighboring voxels shared one of their six faces, an edge is placed between the two corresponding

nodes to connect them. All the nodes in the first cross-sectional slice of the discretized data are considered the top, and all the nodes in the last cross-sectional slice are considered the bottom. To define the min-cut surface, we imagine a continual flow from the top to the bottom where an edge can only transport one "flow unit" at a time. The minimum cut of the min-cut method is the fewest number of edges that can be removed while separating the graph into two regions. The max-flow/min-cut theorem states that the maximal flow at a given time is equal to the size of the minimum cut. The bottleneck points for the maximum flow are the exact edges to be removed for the minimum cut. The min-cut method identifies the smallest grain necks within the sample and thus the region in the snow sample most likely to fail under load due to stress concentration (Salm 1982; Hagenmuller et al. 2014).

As a much simplified case of the min-cut method, consider Figure 1 where the nodes (blue circles) represent a 2-D ice pixel, with the values assigned to the edges (connecting blue lines) in our case representing the size of the necks in between the grains. In other applications, these values can represent myriad other properties (such as flow). To identify the edges to cut, we identify all the minimum values between neighboring nodes and cut the edges at these locations (dotted black line). In three dimensions, the result is a surface that splits the sample into two regions, the top and the bottom, along this minimized path.

Figure 1. Cartoon illustrating min-cut method in 2-D, with *blue dots* representing ice pixels in our case and *blue connecting lines* representing edges. The *dotted black line* on the *right* shows the cut along the minimum edges.

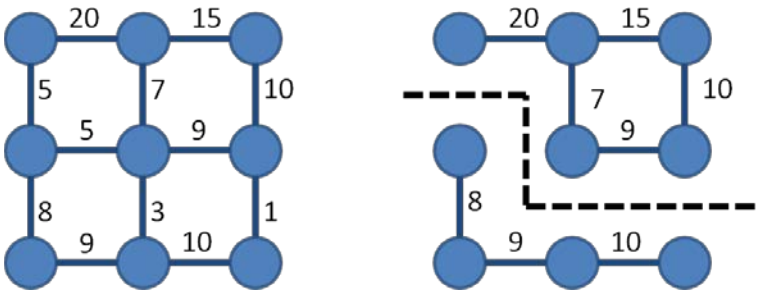

The min-cut algorithm was performed on a 250 × 250 × 100 pixel subset of the data, which represents a 10 mm × 10 mm × 4 mm cube for a total volume of 400 mm^3. Hagenmuller et al. (2014) found that the representative elementary volume (REV), or the minimum volume that adequately represents the phenomena that is being investigated, for the min-cut

method is on the order of 30 to 200 mm^3 for most snow types (excluding hoar crystals and other large, complex grains that are observed in new snow). Our samples with smaller, round ice grains and denser structures represent a more conservative case; and thus, the sample sizes we are investigating are larger than the REV. We observe that the maximum number of edges identified through the min-cut algorithm is equal to the number of pixels in a cross-sectional slice. Thus, we define the "min-cut parameter" to be the fraction of edges identified divided by this theoretical maximum. Since the sample min-cut parameter must be less than or equal to the value for any particular cross-sectional slice, we expect relatively small values for this parameter.

2.3 Compression testing

We performed compression tests using two cold-capable material testing systems (Figure 2) of different scales of strain within the samples as well as sample sizes (i.e., micro- to macroscale). All tests were performed at −10°C. The first, larger system is a Materials Testing System (MTS) on an MTS 311.41 Frame (MTS, Minnesota, United States) equipped with two actuators and three electronically controlled servo valves. The bottom actuator is capable of reaching 1112 kN across a 2286 mm loading surface while the top is able to reach 97.8 kN across a 635 mm loading surface. The top actuator has the ability to be controlled by a two-stage or three-stage servo-valve. These features allow the top actuator to have low load, low displacement, or high speed control loadings. The system is controlled by an MTS FlexTest SE that is connected to a computer running MTS 793 software with the Multipurpose Testware Suite for test procedure design and data collection.

Figure 2. Testing stages used in compaction experiments. *Left*, the CRREL MTS stage with environmental chamber, and *right*, in situ testing stage within the micro-CT scanning chamber.

To test larger samples to failure for compressive-strength determination, we used the MTS stage. All MTS compression tests were conducted at test temperature of −10°C in an environmentally controlled box with a Bemco Series Chiller. The chamber is cooled or heated via closed loop air flow and can hold to within ±0.1 °C. We used strain rates of 14.4×10^{-5} to 5.5×10^{-4} s^{-1} to mimic the conditions for the micro-CT compression stage. We conducted two sets of MTS tests using prepared samples with lower density (average 430 kg/m^3) and higher density (570 kg/m^3) and similar microstructure. The first set of tests used the MTS 4 Post 111 kN two-stage servo-valve with 111 kN load cell; the second set of tests used the MTS 4 post 1112 kN two-stage servo-valve with 111 kN load cell. A total of eight tests at a strain rate of 10.6×10^{-5} s^{-1} of the denser samples were performed to failure to determine compressive strength. Four tests to failure were performed using an extensiometer to accurately determine the strain. Table 3 presents the test matrix. The extensiometer used for these tests was not able to extend to failure for all of the compressive-strength tests; and so in some instances, the strain was calculated from the displacement of the servo-valve actuator instead. The displacement determined from the actuator compares reasonably well to the displacement determined from the extensiometer1, so that the relatively lower accuracy of the actuator does not impact the overall error of the displacement values. All values reported for strain are based on the engineering strain.

Table 3. Test matrix.

Testing System	Strain Rate (s^{-1})	Sample Type	Density (kg/m^3)	# of Replicates
MTS (macroscale)	5.5×10^{-4} to 14.4×10^{-5}	Artificially compacted	442	4
MTS (macrocale)	10.6×10^{-5}	Artificially compacted	520	8
In situ stage (microscale)	15×10^{-5}	Artificially compacted	300–500	4
In situ stage (microscale)	15×10^{-5}	Firn	580	3
In situ stage (microsccale)	15×10^{-5}	Firn	590	6

The second system, the “in situ” stage, is housed inside the micro-CT chamber and is capable of testing relatively small (i.e., 3500 mm^3 cubic volume) samples by using a compression stage while performing pre- and postcompaction microstructural analysis. The in situ stage was used to examine the snow microstructure before and after compression. The in situ

stage has limitations, including the small sample size, a maximum compression length of 6 mm, a maximum load of 445 N, and a set strain rate of $15 \times 10^{-5}\ s^{-1}$. The deformation of snow is strongly influenced by the strain rate (Kinosita 1967). At strain rates lower than 10^{-4} to $10^{-3}\ s^{-1}$, snow deforms plastically and will fracture ductilely, while at higher strain rates, snow is typically brittle (Narita 1980; Schweizer 1998; Kirchner et al. 2001). Past experimental results suggest that the ductile-to-brittle transition is independent of temperature for certain failure modes (Schweizer 1998); for the case of our laboratory tests versus the runway compaction process, our tests were conducted at much higher (a constant −10°C) temperatures compared to the typical operating temperature in Antarctica, which varies considerably over the course of the year.

We performed all tests at low strain rates well below the plastic-to-brittle transition for snow. For the in situ compression tests, the samples were scanned in the micro-CT, compressed 6 mm, scanned again, compressed an additional 6 mm, and scanned again. Time in between compression stages amounted to the time necessary to conduct the scan, which is typically 20–25 minutes. The in situ testing stage does generate heat within the micro-CT chamber during testing; to mitigate these effects, we used a small amount of dry ice in a Styrofoam container to cool the samples during testing (making sure to reset the flat field exposure settings in the chamber before microstructural scanning).

We compared the compaction rates of the micro-CT in situ compression stage and the compaction that occurs during the construction process on the Phoenix Runway. The runway is constructed using a weighted pneumatic tire roller that consists of a 75,000 kg gross weight distributed evenly among four 1 MPa tires with contact areas that are approximately 70 cm long and 125 cm wide. The cart is pulled by a tractor at a top speed of 6 km/h with reported compression tread depths ranging from as much as 15 cm in fresh snow to just faint outlines of the tread pattern during maintenance activities (i.e., <2 cm). The goal of the maintenance activities, as opposed to compaction activities for new snow, is to remediate any loss of density through natural metamorphic processes. Estimating the compaction length as the time it takes for one tire to travel over the contact area and compact the snow 5 cm results in a compaction rate of 0.13 m/s, compared to the compaction rate of the in situ stage, which is a constant set value of 3.3×10^{-6} m/s and obviously much lower than 0.13 m/s. Both

compaction rates are within the plastic limit of snow compaction, and we would expect relatively similar behavior within this range.

Yield strength is determined from experimental data as the interpreted elastic limit in the stress-strain data and the uniaxial compressive strength (UCS) determined from experimental data as the plastic limit at abrupt failure. Young's modulus (E) is determined from experimental data as the yield strength divided by the yield strain.

3 Results

Table 4 summarizes the average sample microstructural characteristics obtained from micro-CT data. The samples were made by compacting snow into cylindrical molds, as discussed in section 2.1, and tested in compression. The first set of tests, designated C1–C7, were compacted to a fixed compaction length. The next round of tests was compacted further to failure and is designated UCS1–UCS10. Samples artificially compacted into large-scale rectangular molds are designated P1; and naturally compacted firn samples from Summit, Greenland are designated Firn1 and Firn2. The density values for the C1–C7 and UCS1–UCS10 samples were calculated using gravimetric means. For the smaller samples tested in the micro-CT, we calculated the densities based on porosity data from the micro-CT analysis due to the high uncertainty in determining the density gravimetrically for the more irregularly shaped low-mass samples. The density, ρ, is related to the porosity, P, multiplied by the density of ice, 917 kg/m^3 (equation [1]):

$$\rho = (1 - P) \text{ x } 917\ kg/m^3 \quad (1)$$

Porosity and SSA are determined from micro-CT data. D_0 is the average optical grain of the snow objects determined from the SSA values, where D_0 = 6/SSA. We examined the stress-strain curves of all the samples to see how well the results from the two different stages compared (Figure 3). In addition, we examined the stress-strain curves of the different types of samples and stages individually with corresponding microstructural characteristics (Figures 4–8).

Table 4. Average sample characteristics before compaction (Precomp) and after compaction (Postcomp).

Sample	Density Precomp (kg/m^3)	Porosity Precomp (%)	Porosity Postcomp (%)	SSA Precomp (mm^{-1})	SSA Postcomp (mm^{-1})	D_0 Precomp (mm)	D_0 Precomp (mm)
C1–C3, C7	442	61.1	39.4	44.4	25.7	0.145	0.24
UCS1–UCS10	520	49.7	33.5	33.5	16.4	0.18	0.37
P1	310	66.2	56.2	56.2	19.9	0.11	0.30
Firn1	580	36.5	31.4	31.4	4.0	0.19	1.50
Firn2	590	36.1	38.3	38.3	4.8	0.16	1.25

3.1 Stress-strain curves

The stress-strain curves produced in the laboratory are shown in Figures 3–8. The engineering strain is reported in all figures. Figure 3 is a comparison of all compression tests that were conducted on both the MTS compression stage (larger samples) and the in situ micro-CT stage (smaller samples) at –10°C. It shows representative samples of both the artificially compacted samples (samples designated C1–C7 and UCS1–UCS10) and the naturally dense firn samples (Firn2). Figure 4 presents results from lower-density compacted samples tested on the MTS that were not conducted to failure; Figure 5 presents results of unconfined compressive-strength tests on the MTS that were conducted to failure. Figures 6–8 present the results of unconfined sample testing using the in situ stage for artificially and naturally compacted snow samples.

Figure 3. Compilation of stress-strain data for both MTS large sample tests (*large diamonds*) and micro-CT small sample tests (*small circles*). Extensiometer-determined strain rate data are displayed for the C1–C7 samples; actuator-determined strain-rate data are displayed for the UCS1–UCS10 samples. The strain rate for the samples tested in the micro-CT scanner was determined by the movement of the materials testing stage.

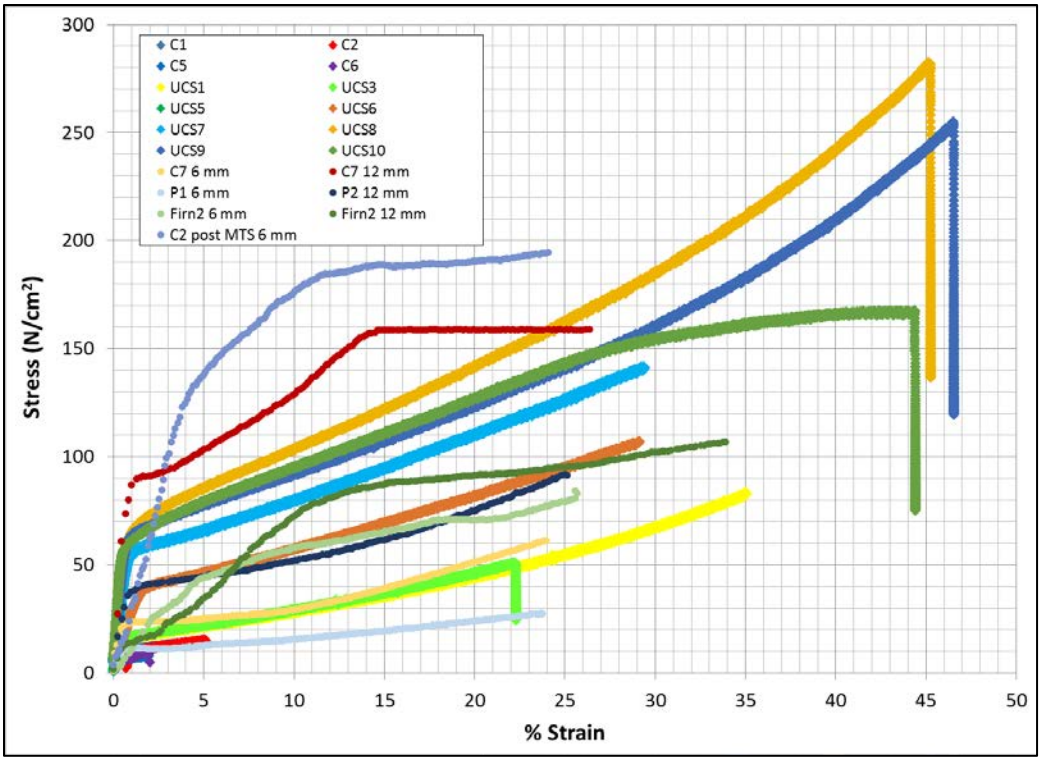

Figure 4. MTS unconfined data for low-density samples, with an average density of 430 kg/m³ ± 15 kg/m³.

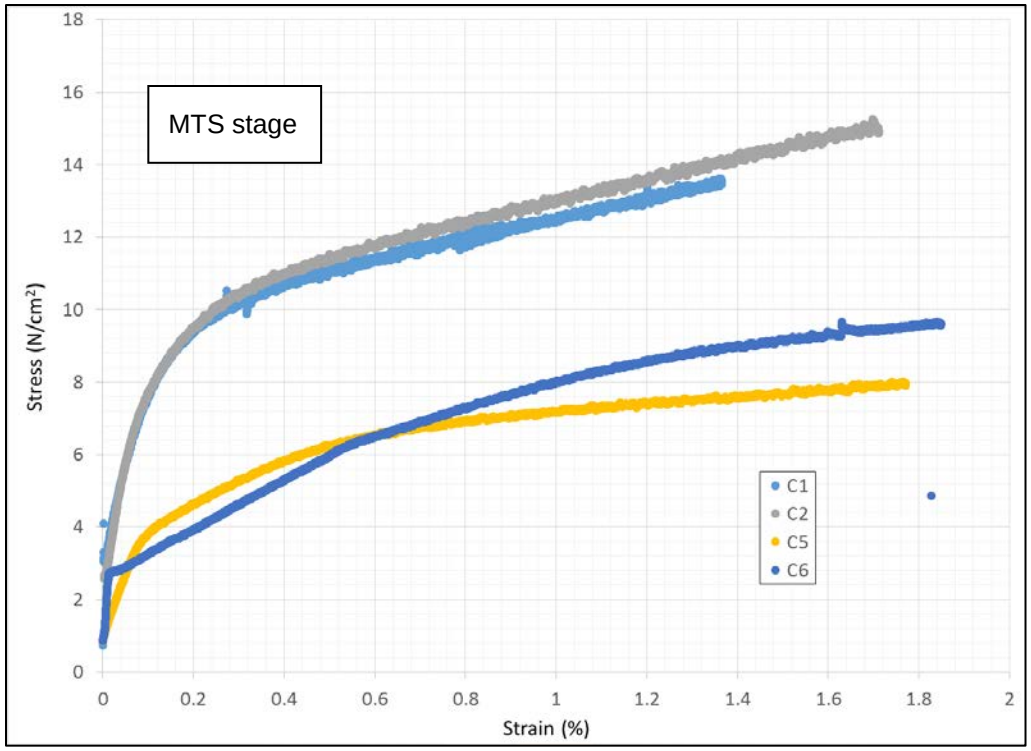

Figure 5. Uniaxial compressive-strength tests in the MTS. These samples were all prepared in the same manner, with an average density of 570 kg/m³ ± 13 kg/m³. Tests UCS6, and UCS7 were not performed to failure due to equipment issues.

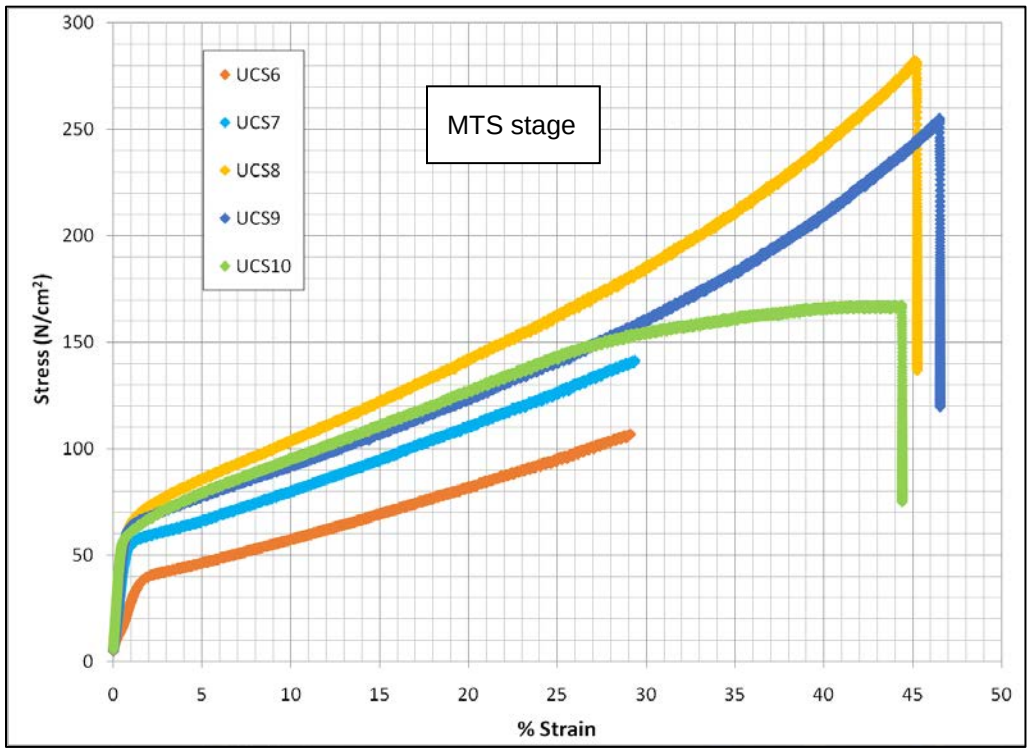

Figures 4 and 5 exhibit considerable variation in stress-strain relationships, considering that the samples in each plot were made in an identical fashion to one another. Figure 4 demonstrates strain weakening, while Figure 5 demonstrates strain hardening. This suggests that there are variations among the four samples not captured by density differences (i.e., most likely in sample-end preparation and the degree to which the sample ends are parallel, which can be due to the high number of asperities that naturally exist in snow). It is also possible that localized failure within samples C6 and C5 leads to different overall behavior compared to samples C1 and C2. Figure 5 shows similar differences in samples that were created identically to one another. Compared to other results (i.e., Landauer 1955) that similarly demonstrated a range of behavior for identically prepared specimens of lower density, the stress-strain curves obtained in this examination demonstrate an interesting behavior at high strain rates, where an approximately constant stress level is typically reached.

The in situ stage is limited to a fixed strain rate and maximum stage travel distance (6 mm max compressive distance), so we conducted tests consisting of one compression to a 6 mm compaction, scanned the sample to determine microstructure characteristics resulting from this compaction, and compressed an additional 6 mm to reach of a total of 12 mm displacement (Figure 6). This allowed us to compact greater amounts and to perform intermediate microstructural scans (Figures 7 and 8 with corresponding microstructural data inset) pre- and postcompaction. Time in between compression stages was equal to the typical time the micro-CT scan took to complete, usually 20–25 minutes. The percentage of strain reported in each figure is the strain due to each individual 6 mm compression cycle and not the overall total strain of the sample. Also note that for the case of sample C7, the top platen of the compression stage was not in contact with the sample, resulting in artificially high strain rates until the platen contacted the sample top again. The friable nature of snow results in a high number of asperities at the sample surface, which contributes to the large variation in test results.

Figure 6. Unconfined compressive stress-strain curves of artificially compacted samples from the in situ micro-CT materials testing stage, with samples of a range of densities and preparations, compacted 6 mm and 12 mm. Strain percentage is reported as the strain per compaction cycle and not the overall strain of the sample.

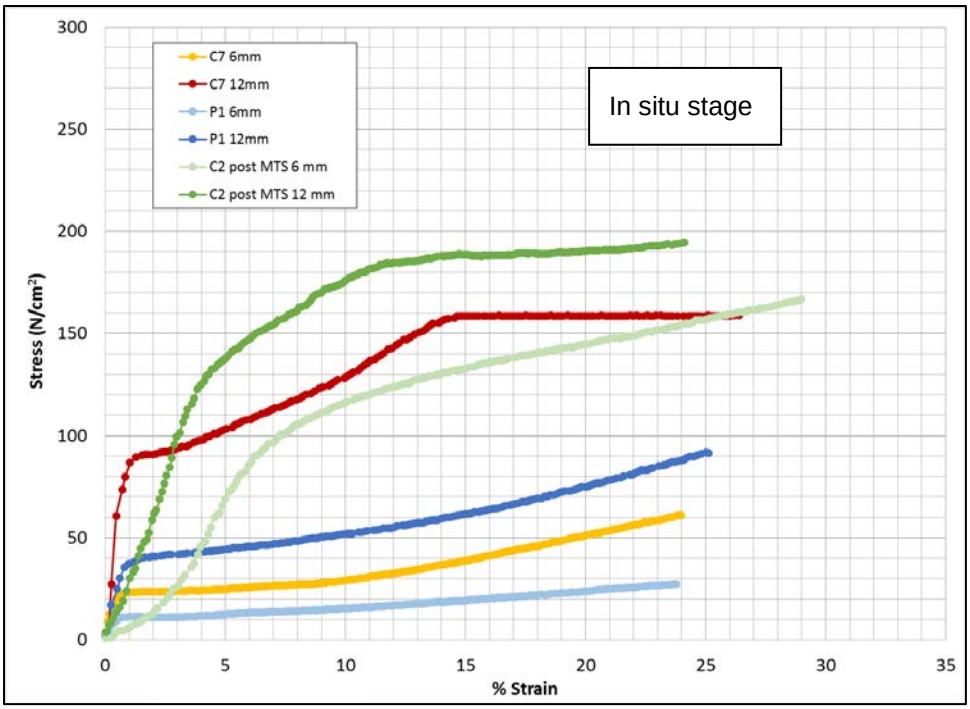

Figure 7. Unconfined compressive stress-strain curves of artificially compacted samples from the in situ micro-CT materials testing stage compacted first 6 mm and then an additional 6 mm for a total of 12 mm reduction in sample height, with resulting 3-D microstructural scans (*inset*) of the P1 (large sample).

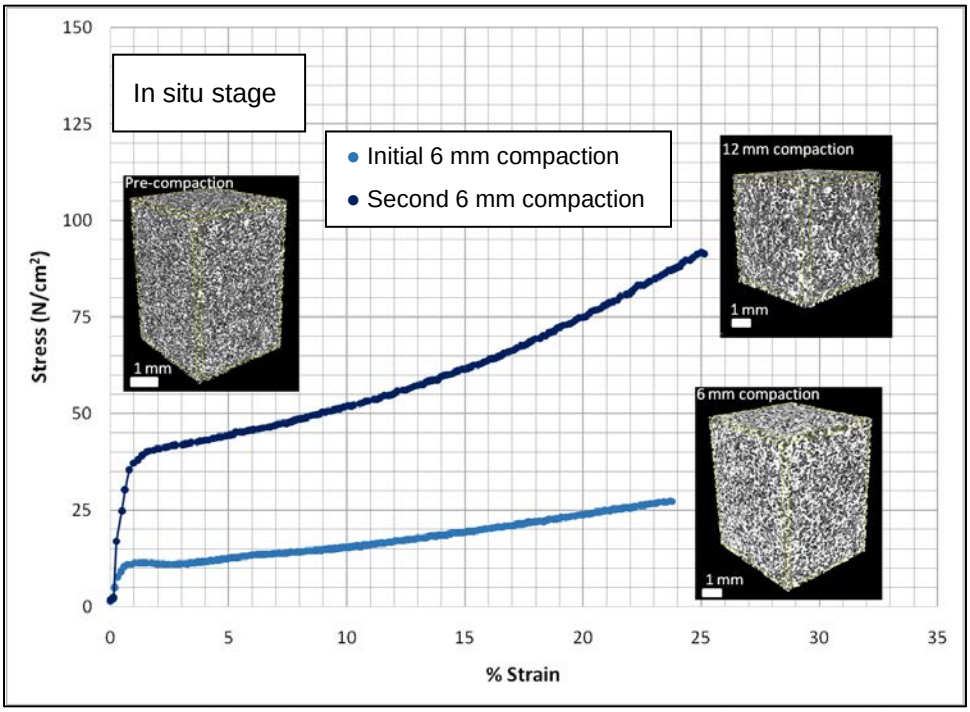

Figure 8. Unconfined compressive stress-strain curves for polar firn samples tested in the in situ stage.

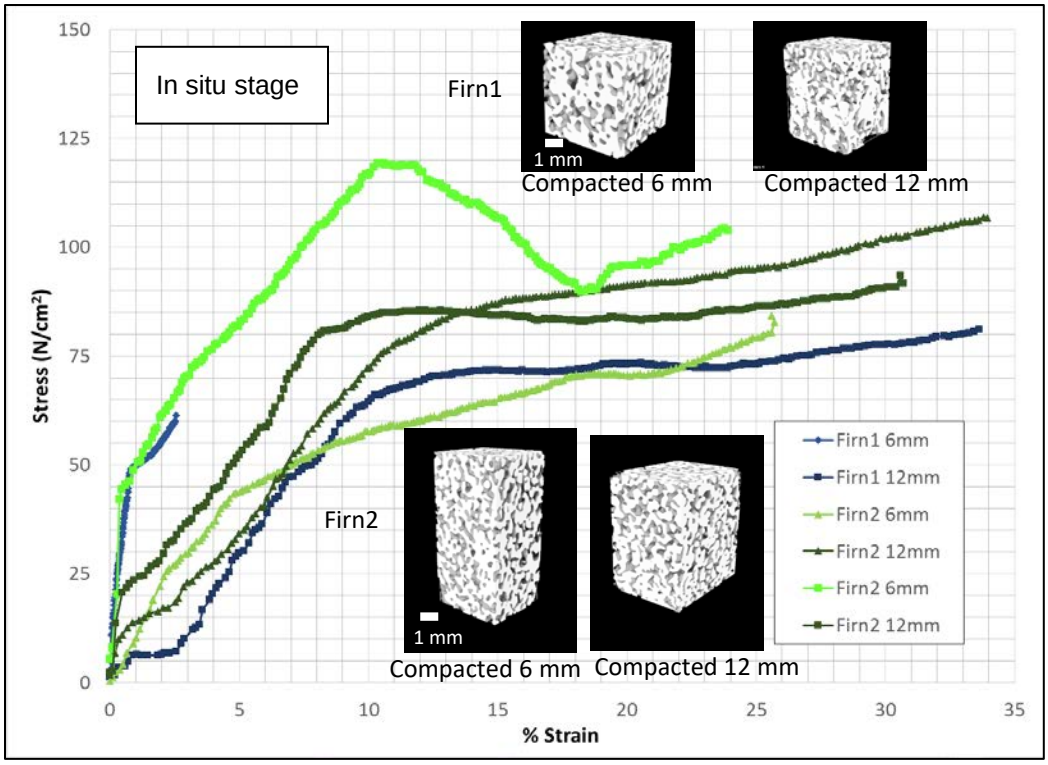

As can be expected, the yield stress for the artificially precompacted samples (i.e., those that have been compacted 6 mm and then, after 20 minutes to allow for micro-CT scanning to take place, compacted an additional 6 mm) demonstrates a much higher strength (Figures 6 and 7). Samples compacted a second time have yield strengths three to four times higher than after the first compaction. The results for the naturally dense firn samples are much more variable (Figure 8) and exhibit higher yield stress after the first compaction stage when compared to the yield stress of the second compaction stage for some samples.

The uniaxial compressive strength as a function of density for samples that were tested to failure is shown in Figure 9 and is summarized in Table 5. The compressive strength increases by a factor of five with increasing density from 420 to 600 kg/m^3.

Figure 9. Strength at failure versus density.

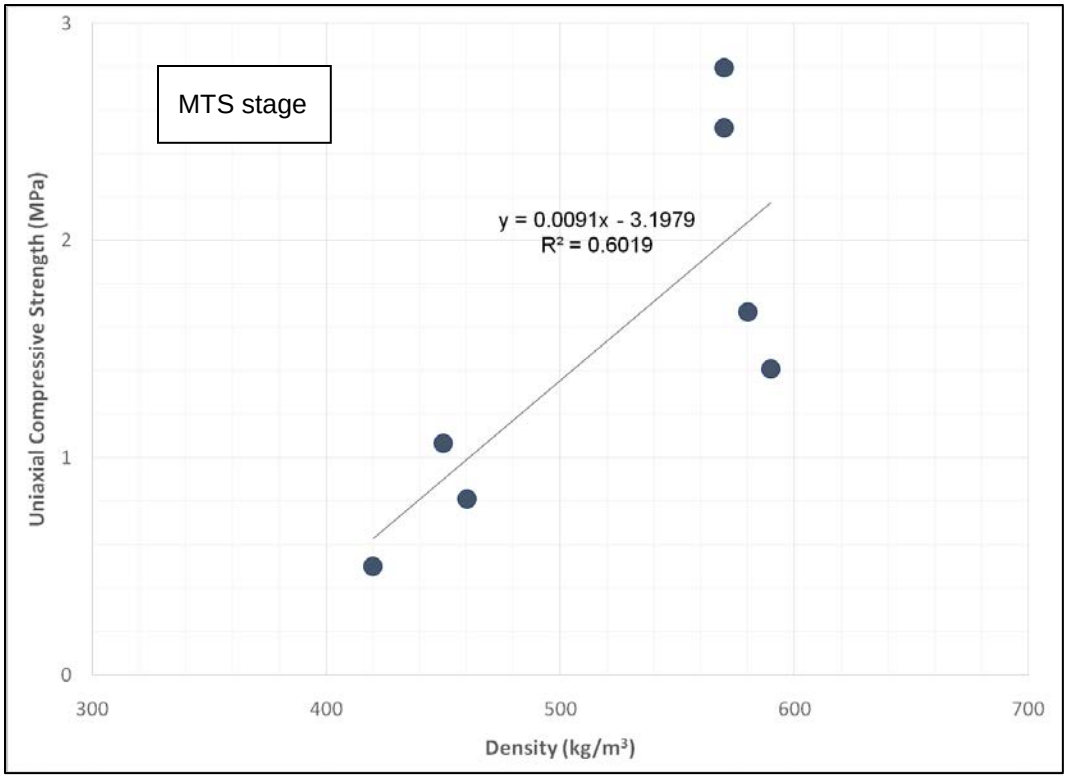

Table 5. Uniaxial compressive-strength results.

Sample	Density (kg/m³)	Uniaxial Compressive Strength (MPa)
UCS1	460	0.81
UCS3	420	0.50
UCS6	450	1.07
UCS7	590	1.41
UCS8	570	2.79
UCS9	570	2.52
UCS10	580	1.67
Average	520	1.54
Standard Deviation	73	0.86

3.2 Microstructure evolution

3.2.1 Porosity during compression

Figure 10 shows the evolution of the snow total porosity (i.e., the open and closed porosity combined) during compression in the in situ compression stage in the micro-CT. The total porosity decreases as the snow is com-

pressed for all samples. The compaction at 6 mm corresponds to an engineering strain rate, on average, of 28% while the compaction to 12 mm corresponds to an average engineering strain rate of 43% overall when compared to the original sample.

Figure 10. Evolution of porosity during compression. A compaction of 6 mm corresponds to an average engineering strain rate of 28% while a compaction of 12 mm corresponds to an overall engineering strain rate of 43%.

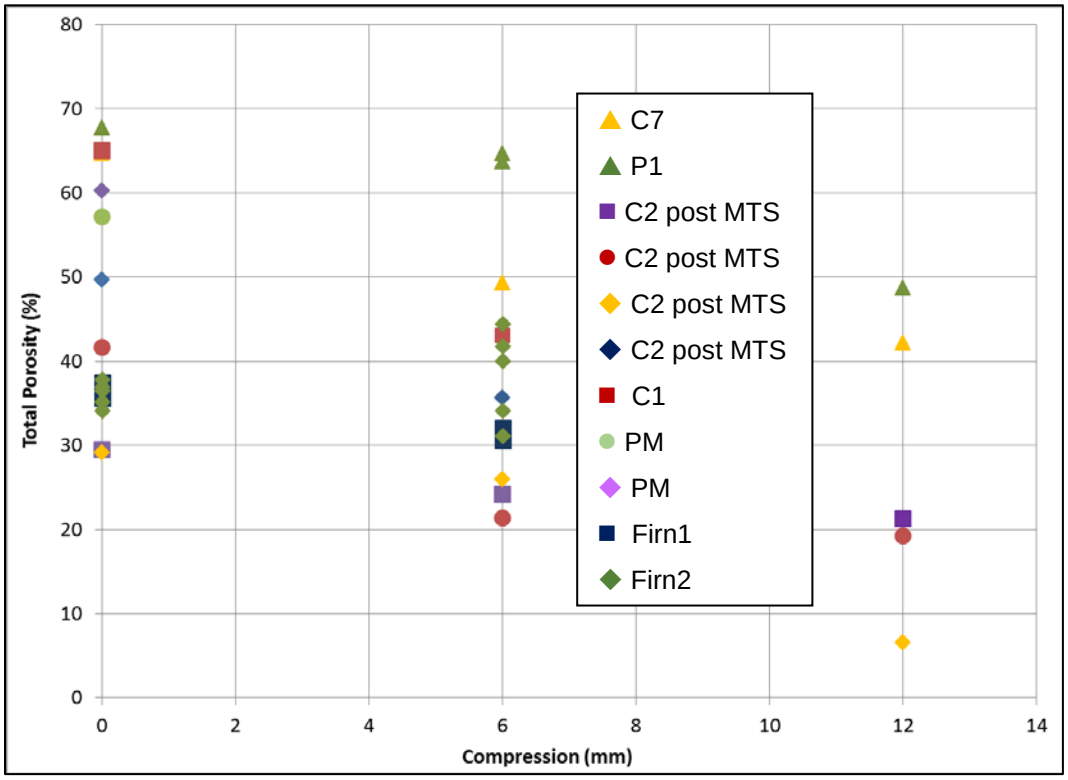

3.2.2 Surface-to-volume ratio during compression

Figure 11 shows the evolution of the surface-to-volume ratio (S/V ratio) during compression for the various types of samples along with 2-D cross sections of the microstructural analysis for each type of sample. The S/V ratio for the artificially compacted snow samples decreases approximately 15%–20% as the samples are compressed 6 mm and then to a total of 12 mm, with corresponding increase in the ice-grain size. The changes in snow structure are apparent visually in the reconstructed micro-CT data (Figure 11, bottom) with an increase in the connected ice-grain structure during snow compaction reflected in trends of the S/V ratio.

Figure 12 shows the evolution of the ice S/V ratio for artificially compacted versus naturally compacted snow and compares the samples constructed in a large mold (P1) to the firn samples (Firn1 and Firn2).

Figure 11. The evolution of the snow surface-to-volume (S/V) ratio during compaction. Two-dimensional cross sections of the ice microstructure are shown (*bottom*) to illustrate the changes in snow structure.

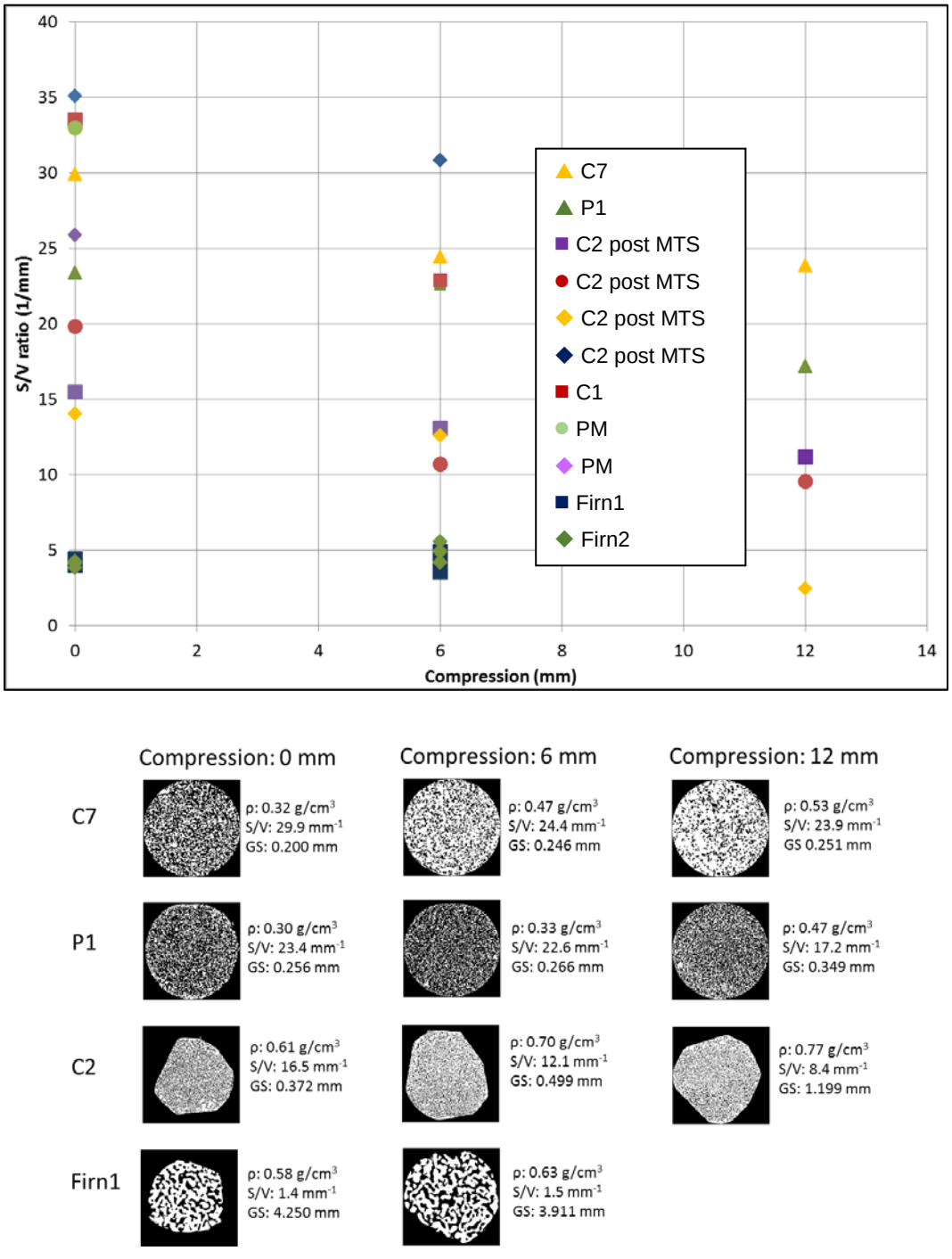

Figure 12. Evolution of the snow S/V ratio during compression of artificially compacted samples (*top*) and naturally compacted samples (*bottom*) (note differences in scales).

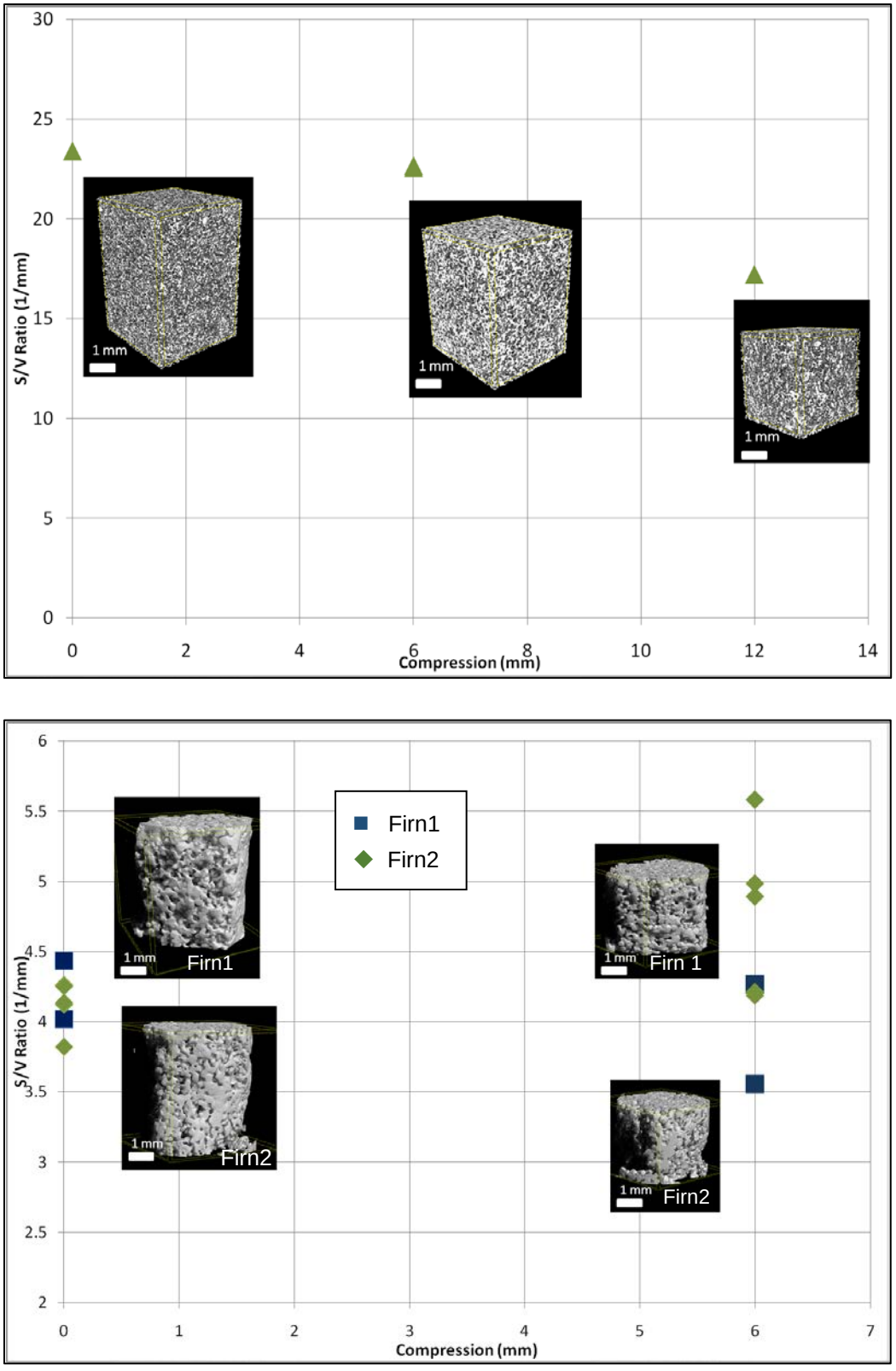

The P1 sample had a low starting density (310 kg/m^3) compared to the firn samples, with densities of 580 and 590 kg/m^3, respectively, for the density of the Firn1 and Firn2 samples. The figure shows the 3-D snow micro-CT data for comparison. The S/V ratio decreases much faster for P1 artificially compacted samples than for the firn samples, which have relatively constant low S/V ratios throughout the compaction testing. We speculate that the low, constant S/V ratio is due to the well-established ice matrix in the firn caused by extensive metamorphism and long residence time at depth exhibited by the naturally compacted snow. In these naturally compacted snow samples, large ice necks connect the ice phase, compared to the smaller necks in the artificially compacted snow. The min-cut values for the firn samples are an order of magnitude higher than the artificially compacted samples. We speculate that the longer the snow structure is allowed to sinter, the stronger it will become due to the development of larger grain neck structures.

4 Discussion

4.1 Comparison to published results

4.1.1 Elastic modulus

Shapiro et al. (1997) correlates snow elastic modulus and snow density for strain rates that vary from 3×10^{-3} to 2×10^{-2} s^{-1} at −25°C. Haehnel (2017) compiled a look-up table to characterize the change in elastic modulus with snow density (Table 6) based on the data of Shapiro et al. (1997) and further developed a correlation for calculating the Elastic modulus, *E*, from snow density:

$$E(\text{MPa}) = 8 \times 10^{-14} \rho \left(\frac{\text{kg}}{\text{m}^3}\right)^{5.81} \quad (2)$$

Table 6. Dependency of elastic modulus on snow density (Shapiro et al. 1997) from Haehnel (2017).

Snow Density (kg/m³)	Elastic Modulus (MPa)
200	1.379
380	98.20
410	146.9
470	303.3
540	633.6
620	1319.0
770	4165.0
900	9532.0

When the values of elastic moduli determined for the uniaxial compressive tests UCS1–UCS10 are plotted vs. density and compared to previous results (Figure 13) as summarized in Shapiro (1997), our results compare best to the results of Kuvaeva et al. (1967) who conducted static and quasi-static measurements of Poisson's ratio (line "K" in Figure 13). The low strain rate of our compression tests (1.5×10^{-6} s^{-1}) compared to the strain rate of the compression tests conducted by Kovacs et al. 1969 (curve "B" in Figure 13) is one possible explanation for the differences; but they are likely due to other differences, including microstructural variations induced from the construction process (i.e., our samples had small grains compared to natural snow samples). Our results show different behavior

when compared to earlier work conducted by Landauer (1955), who calculated a Young's modulus of 160 MPa for snow of density 0.42 kg/cm^3 at constant displacement velocities of 10^{-5} s^{-1} and 10^{-3} s^{-1}.

Figure 13. From Shapiro et al. (1997), Young's modulus vs. density for dry, coherent snow (modified from Fig. 2 in Mellor 1975). Data sources cited in the original figure are (*A*) pulse propagation or flexural vibration at high frequencies, –10° to –25°C (Smith 1965; Nakaya 1959a, b; Bentley et al. 1957; Crary et al. 1962; Lee 1961; Ramseier 1963); (*B*) uniaxial compression, strain rate approximately 3 × 10^{-3} to 2 × 10^{-2} s^{-1}, temperature –25°C (Kovacs et al. 1969); (*C1*) uniaxial compression and tension, strain rate approximately 8 × 10^{-6} to 4 × 10^{-4} s^{-1}, –12° to –25°C; (*C2*) static creep test, –6.5° to –19°C (Kojima 1954); (*D*) complex modulus, 103 Hz, –14°C (Smith 1969); and (*K*) plotted from the equation for best fit curve to data for static Young's modulus and quasi-static measurements of Poisson's ratio from Kuvaeva et al. (1967).

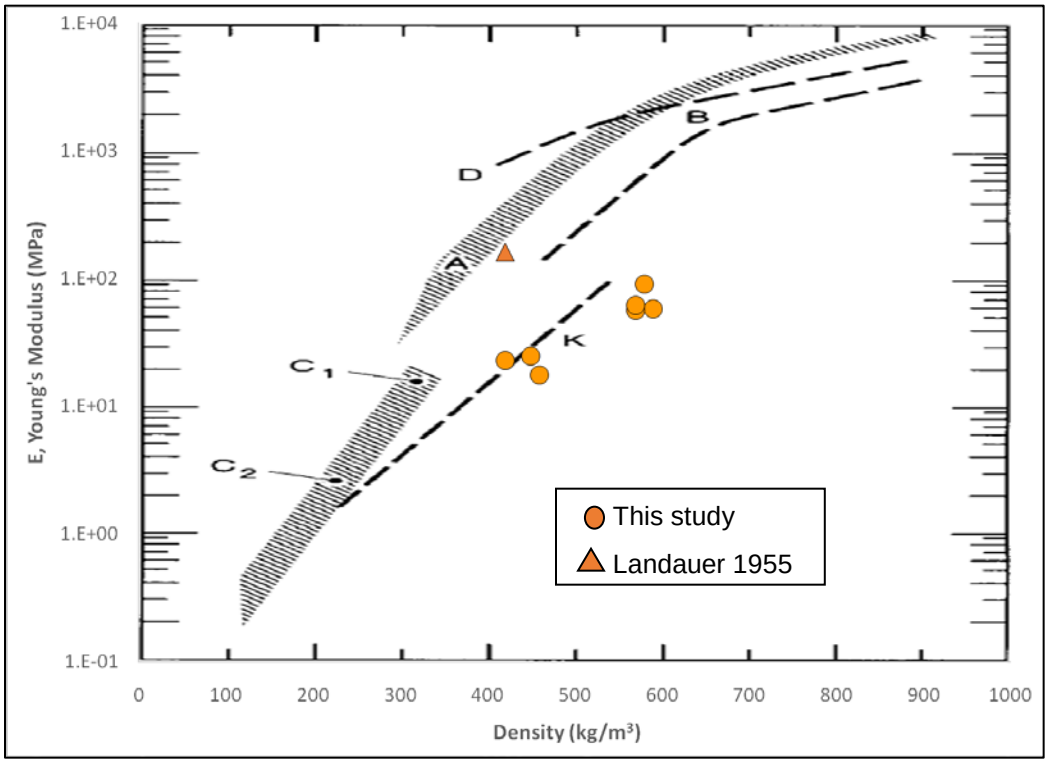

4.1.2 Compressive failure strength

Few results for high-density compressive strength at low strain rates exist, so we compared our results to those of Lintzén (2012), who examined the compressive strength of artificially compacted snow used to construct the ICEHOTEL in Jukkasjärvi, Sweden (Figure 14). Our results compare relatively well to their results, with the snow samples we constructed having higher compressive strength per density. This is not surprising given the extreme construction techniques we used (i.e., heavy compaction) to replicate the Phoenix runway samples.

Figure 14. Uniaxial compressive strength vs. density for lab samples in this study with results of compressive-strength tests from Lintzén 2012. The deformation rates for the Lintzén tests, 0.5 mm/s to 5 mm/s, are much faster than the deformation rates for this study, 0.003 mm/s in the micro-CT and 0.002 mm/s in the MTS.

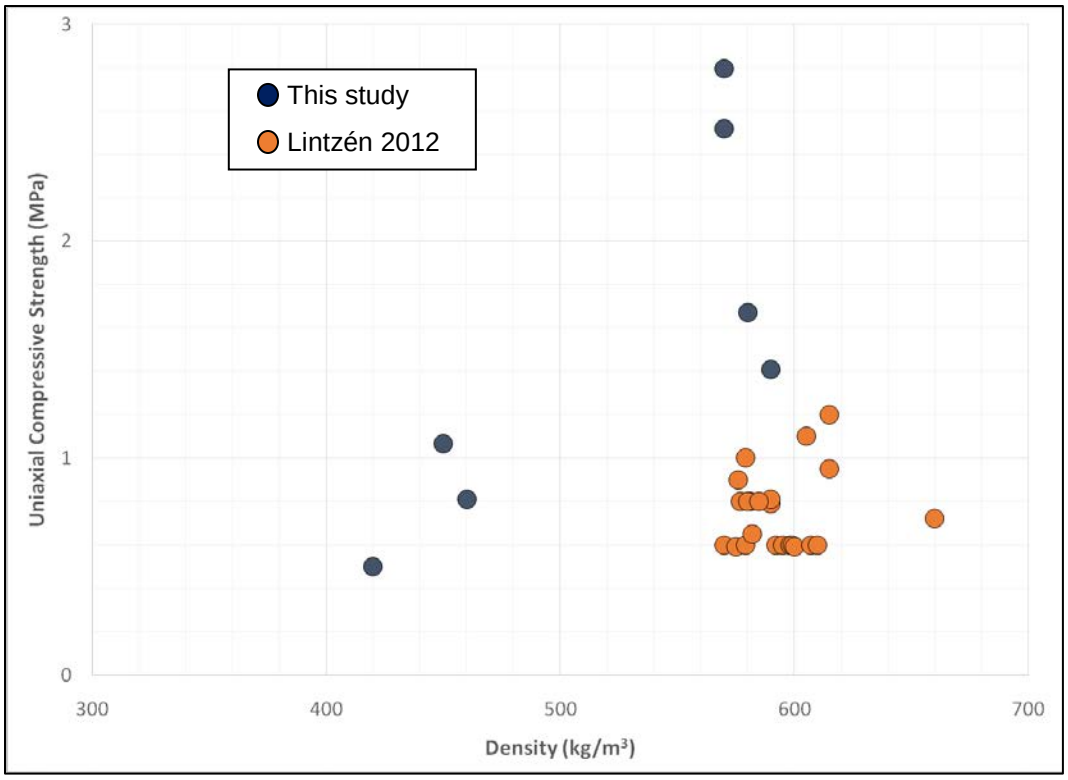

Shapiro et al. (1997) provide the most comprehensive review of snow compressive-strength results for a range of snow densities (Figure 15). However, most of these values were determined at high strain rates in the brittle regime. The Lintzén (2012) tests were conducted at low strain rates in the plastic regime and at high densities (i.e., 560 to 660 kg/m^3) comparable to the samples from our study. Our values compare well with the compilation of past historical results, with the values of the samples we constructed being slightly higher than the results of the Mellor (1975) compilation results at higher strain rates (and brittle failure) (Figure 15).

Figure 15. Stress-strain curves of artificially compacted samples from the in situ micro-CT materials testing stage (*orange dots*) from this study, with samples of a range of densities and preparations from historical work. Figure modified from Shapiro et al. (1997).

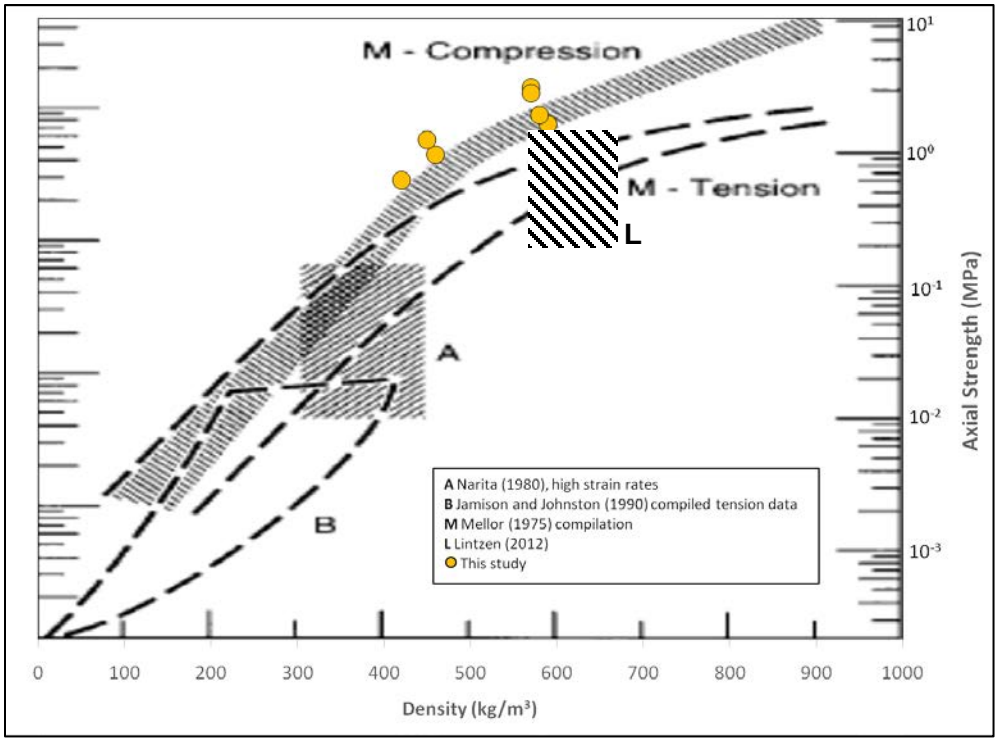

4.2 Microstructural parameterizations of snow strength

In this section, we compare the standard density parameterizations of snow strength to min-cut parameterizations of snow strength. As a first step in the parameterizations, we examine the straight-line best fit of the data, normalized by the total range of each parameter for comparison (Figure 16), for both density and the min-cut parameter computed from the micro-CT 3-D microstructure data.

4.2.1 Density vs. min-cut parameterizations of strength

Figure 16 illustrates the straight-line parameterizations of density and min-cut for the data, further summarized in Table 7. We examine the relationships between density (Figure 16, top) and min-cut (Figure 16, bottom) for the microstructural and strength data of interest, including the min-cut parameter (min-cut), the specific surface area of the ice phase (SSA), Young's modulus (E), yield strength, and the uniaxial compressive strength (UCS) determined from experimental data.

Figure 16. Dimensionless density parameterizations of snow strength and microstructural properties (*top*) and dimensionless min-cut parameterizations (*bottom*) normalized over the range of each parameter. SSA is the ice phase specific surface area, *E* is Young's modulus, and UCS is the uniaxial compressive strength.

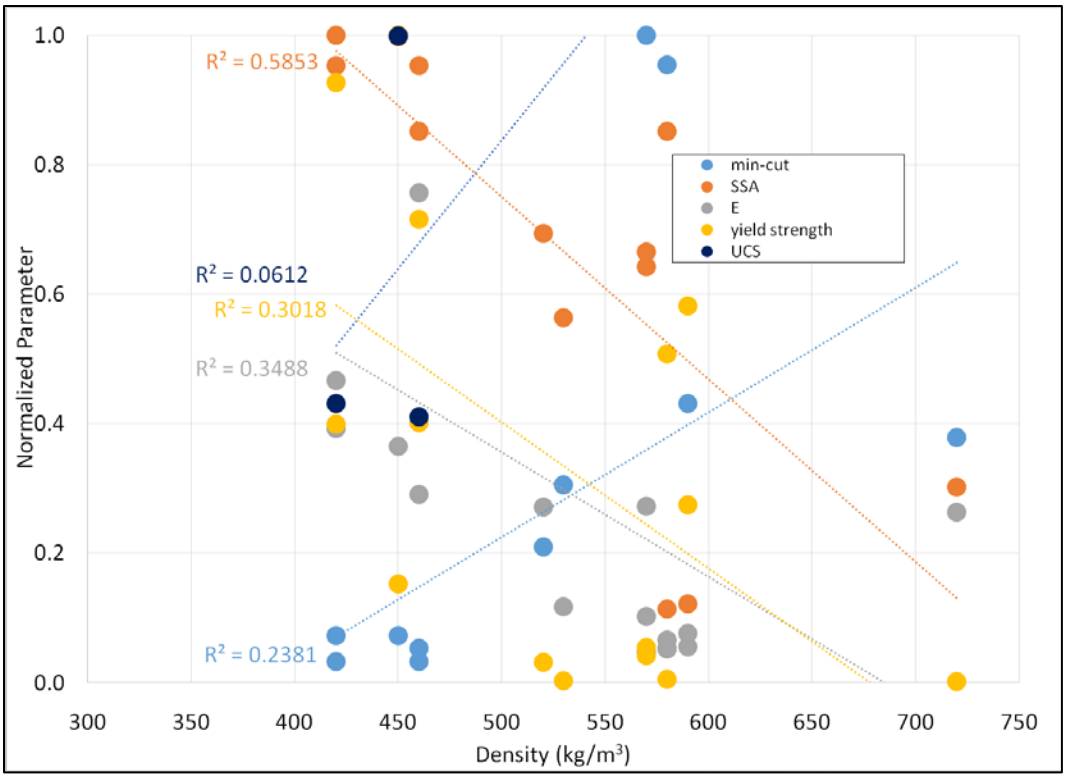

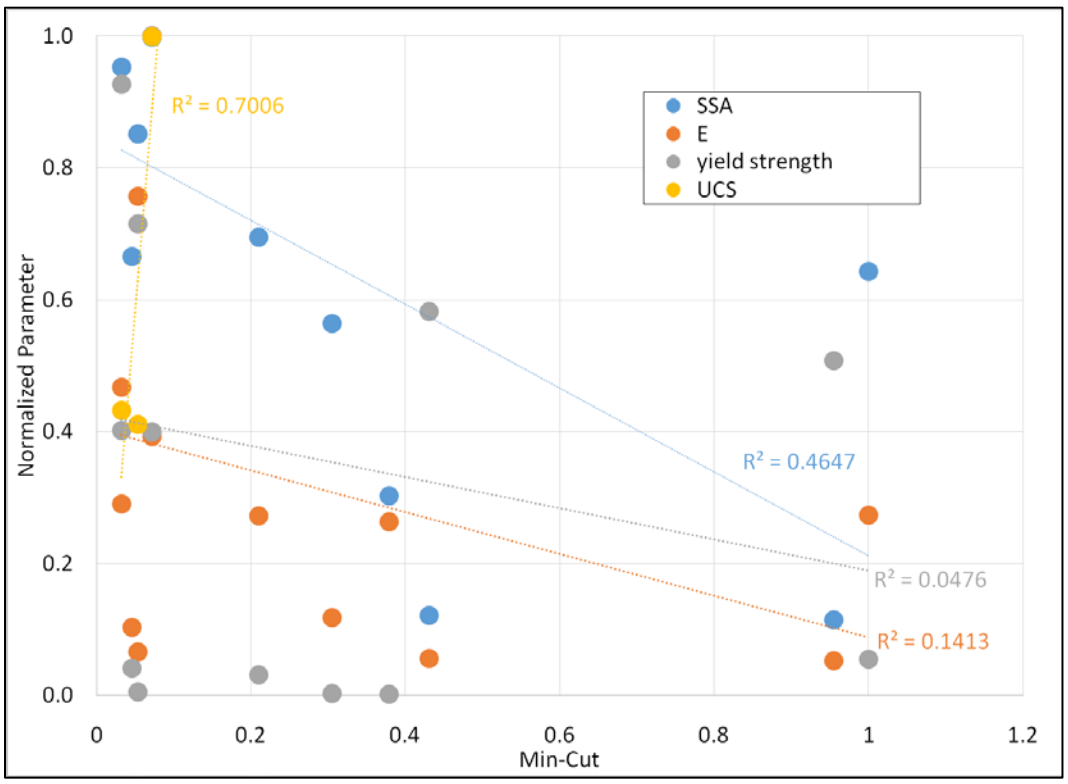

Table 7. Density (ρ) vs. min-cut (c) parameterizations of snow strength elastic modulus, yield strength, uniaxial compressive strength (UCS), and specific surface area (SSA)

Density Parameterizations (ρ)			Min-Cut Parameterizations (c)		
Parameter	Equation	R^2	Parameter	Equation	R^2
Min-cut	$0.0018\rho - 0.7033$	0.24			
SSA	$-0.1079\rho + 82.701$	0.59	SSA	$-25.6c + 32.5$	0.46
Elastic modulus	$-0.2056\rho + 140.87$	0.35	Elastic modulus	$-35.6c + 43.4$	0.14
Yield strength	$-0.0555\rho + 37.643$	0.30	Yield strength	$-6.1c + 10.5$	0.05
UCS	$0.1455\rho - 41.976$	0.06	UCS	$539.3c - 4.6$	0.70

Using power law or logarithmic fits of the data does improve the fit to the elastic modulus and yield stress data, but not appreciably (R^2 improves from 0.35 to 0.43 for the elastic modulus and from 0.30 to 0.39 for the yield strength), and similarly for the min-cut parameterizations.

4.2.2 Microstructure parameterizations based on density and min-cut

The specific surface area of the ice grains is related to the density of the snow samples, as based ultimately on the packing factor of the snow (i.e., rounded, smaller ice grains tend to pack more densely than larger, more complicated snow structures). The min-cut parameter is not as well parameterized by density. The SSA of the snow specimens is slightly better parameterized by density vs. the min-cut values, demonstrating that there is some correlation between the ice-grain size and min-cut parameter.

4.2.3 Elastic modulus, yield strength, and unconfined compressive strength

In our study, the elastic modulus and the yield strength are best parametrized by the density of the samples and not as well by the min-cut values we computed from the micro-CT data. We do see an improvement in the parameterization of the unconfined compressive strength using the min-cut parameter vs. the density.

5 Conclusions

The main objective of this work was to determine from micro-CT data analysis the microstructural parameters calculated that best predict corresponding snow strength. We conducted compression tests for a range of high-density snow samples constructed to mimic the snow pavement system of the Phoenix Runway. We were able to approach, but not duplicate, the very high snow densities of the as-constructed runway by using our sample preparation methodology in the laboratory. Nevertheless, our results of multistep compaction processes help elucidate some of the processes likely occurring on the runway in which new snow is incorporated into the runway surface through several compaction passes.

Our coupled snow strength–snow microstructure examinations indicate that the min-cut parameter calculated from the 3-D microstructure data has potential to better parameterize snow compressive failure strength and lead to a physically meaningful microstructural determination of snow failure. Snow density does relate better than the min-cut parameter to snow yield strength and snow elastic modulus in our study for the limited number of samples examined. Low-density snow structures develop strength through repeated compaction processes much more quickly than higher-density snow structures, as to be expected. Our results indicate that new parameterizations of snow strength, based on microstructural information, have the potential to improve snow strength predictions with future investigations of larger sample numbers warranted, particularly in the investigation of the elastic deformation of snow.

References

Abele, G. 1968. *An Experimental Snow Runway Pavement in Antarctica*. CRREL TR 211. Hanover, NH: U.S. Army Cold Regions Research and Engineering Laboratory.

———. 1990. *Snow Roads and Runways*. CRREL Monograph 90-3. Hanover, NH: U.S. Army Cold Regions Research and Engineering Laboratory.

Aver'yanov, V. G., V. D. Klokov, G. Y. Klyuchnikov, Y. S. Korotkevich, and V. N. Petrov. 1983. Construction of Snow Airstrips for Wheeled Aircraft in the Antarctic. *Polar Geography and Geology* 9 (1): 37–41.

Bentley, C. R., P. W. Pomeroy, and H .J. Dorman. 1957. Seismic Measurements on the Greenland Ice Cap. *Annals of Glaciology* 13:253–285.

Crary, A. P., E. S. Robinson, H. F. Bennett, and W. W. Boyd. 1962. *Glaciological Studies of the Ross Ice Shelf, Antarctica, 1957–1960*. IGY Glaciological Report no. 6. New York: American Geographical Society.

Gerling, B., H. Lowe, and A. van Herwijnen. 2017. Measuring the Elastic Modulus of Snow. *Geophysical Research Letters* 44 (11): 11,088–11,096. https://doi.org/10.1002/2017GL075110.

Haehnel, R. B. 2017. *A Creep Model for High-Density Snow*. ERDC/CRREL TR-17-7. Hanover, NH: U.S. Army Engineer Research and Development Center.

Haehnel, R. B., K. L. Bjella, M. A. Knuth, L. A. Barna. 2013. *McMurdo Consolidated Airfields Study: Phase 1*. ERDC/CRREL TR-13-5. Hanover, NH: U.S. Army Engineer Research and Development Center.

Haehnel, R. B., K. A. Knuth, T. D. Melendy, C. A. Hiemstra, and R. E. Davis. 2014. *Design and Implementation of a Consolidated Airfield at McMurdo, Antarctica*. ERDC/CRREL TR-14-22. Hanover, NH: U.S. Army Engineer Research and Development Center.

Hagenmuller, P., N. Calonne, G. Chambon, F. Flin, C. Geindreau, and M. Naaim. 2014. Characterization of the Snow Microstructural Bonding System through the Minimum Cut Density. *Cold Regions Science and Technology* 108:72–79. https://doi.org/10.1016/j.coldregions.2014.09.002.

Jamison, J. B., and C. D. Johnston. 1990. In-Situ Tensile Tests of Snow-Pack Layers. *Journal of Glaciology* 36 (122): 102–106.

Kinosita, S. (1967). Compression of Snow at Constant Speed. In *Physics of Snow and Ice: Proceedings of the International Conference on Low Temperature Science*, 14–19 August 1966, Sapporo, Japan, 1 (2): 911–927. http://hdl.handle.net/2115/20350.

Kirchner, H.O. K., G. Michot, H. Narita and T. Suzuki. 2001. Snow as a Foam of Ice: Plasticity, Fracture and the Brittle-to-Ductile Transition. *Philosophical Magazine A* 81 (9): 2191–2181. https://doi.org/10.1080/01418610108217141.

Kojima, S. 1954. Viscoelastic Property of Snow. *Low Temperature Science, Series A* 12:1–13.

Kovacs, A. F., W. F. Weeks, and F. Michitti. 1969. *Variation of Some Mechanical Properties of Polar Snow, Camp Century, Greenland*. Research Report 276. Hanover, NH: U.S. Army Cold Regions Research and Engineering Laboratory.

Kuvaeva, G. M., G. K. Sulakvelidze, V. S. Chitadze, L. S. Chotorlishvili, and A. M. El'Mesov. 1967. *Physical Properties of Snow Cover of the Greater Caucasus Mountains*. Translation, Indian National Science Document Center (1975).

Landauer, J. K., 1955. Stress-Strain Relations in Snow under Uniaxial Compression. *Journal of Applied Physics* 26 (12): 1493–1497.

Lee, T. M. 1961. *Note on Young's Modulus and Poisson's Ratio of Naturally Compacted Snow and Processed Snow*. CRREL Technical Note. Hanover, NH: U.S. Army Cold Regions Research and Engineering Laboratory.

Lintzén, N. 2012. Compression Strength of Snow—Experimental Measurements at ICEHOTEL in April 2012. Dissertation, Lulea Tekniska Universitet, Lulea, Sweden.

Mellor, M. 1975. A Review of Basic Snow Mechanics. In *The International Symposium on Snow Mechanics*, Grindelwald, Switzerland, 1–5 April 1974, IAHS-AISH Publication 114: 251–291.

———. 1993. *Notes on Antarctic Aviation*. CRREL Report 93-14. Hanover, NH: U.S. Army Cold Regions Research and Engineering Laboratory.

Moser, E. H., and G. E. Sherwood. 1968. The Load-Carrying Capacity of Depth-Processed Snow on Deep Snowfields. In *Physics of Snow and Ice: Proceedings of the International Conference on Low Temperature Science*, 14–19 August 1966, Sapporo, Japan, 1 (2): 993–1005. http://hdl.handle.net/2115/20355.

Nakaya, U. 1959a. *Viscoelastic Properties of Snow and Ice in the Greenland Ice Cap*. Research Report 46. Wilmette, IL: U.S. Army Snow Ice and Permafrost Research Establishment.

———. 1959b. *Viscoelastic Properties of Processed Snow*. Research Report 58. Wilmette, IL: U.S. Army Snow Ice and Permafrost Research Establishment

Narita, H. 1980. Mechanical Behavior and Structure of Snow under Uniaxial Tensile Stress. *Journal of Glaciology* 26 (94): 275–282.

Petrovich, J. J. 2003. Review: Mechanical Properties of Snow and Ice. *Journal of Materials Science* 38:1–6. https://doi.org/:10.1023/A:1021134128038.

Ramseier, R. O. 1963. Some Physical and Mechanical Properties of Polar Snow. *Journal of Glaciology* 5 (39): 325–332.

Reiweger, I., and J. Schweizer. 2010. Failure of a Layer of Buried Surface Hoar. *Geophysical Research Letters* 37 (24): L24501. https://doi.org/10.1029/2010GL045433.

Russell-Head, D. S., and W. F. Budd. 1989. *Compacted Snow Runways: Guidelines for Their Design and Construction in Antarctica*. CRREL Special Report 89-10. Hanover, NH: U.S. Army Cold Regions Research and Engineering Laboratory.

Salm, B. 1982 Mechanical Properties of Snow. *Reviews of Geophysics* 20(1): 1–19. https://doi.org/10.1029/RG020i001p00001.

Schweizer, J. 1998. Laboratory experiments on shear failure of snow. *Annals of Glaciology* 26:97–102. https://doi.org/10.3189/1998AoG26-1-97-102.

Smith, J. L. 1965. *The Elastic Constants, Strength and Density of Greenland Snow as Determined from Measurements of Sonic Wave Velocity*. CRREL Technical Report 167. Hanover, NH: U.S. Army Cold Regions Research and Engineering Laboratory.

Smith, N. 1969. *Determining the Dynamic Properties of Snow and Ice by Forced Vibration*. ERDC/CRREL Technical Report 216. Hanover, NH: U.S. Army Cold Regions Research and Engineering Laboratory.

Shapiro, L., J. Johnson, M. Sturm, and G. Blaisdell. 1997. *Snow Mechanics: Review of the State of Knowledge and Applications*. CRREL Report 97-3. Hanover, NH: U.S. Army Cold Regions Research and Engineering Laboratory.

Tabor, Z. 2007. Optimal Cut of Trabecular Network. *Medical Engineering and Physics* 29:298–306. https://doi.org/10.1016/j.medengphy.2006.04.001.

Van Herwijnen, A., J. Gaume, E. H. Bair, B. Reuter, K. W. Birkeland, and J. Schweizer. 2016. Estimating the Effective Elastic Modulus and Specific Fracture Energy of Snowpack Layers from Field Experiment. *Journal of Glaciology* 62 (236): 997–1007. https://doi.org/10.1017/jog.2016.90.

REPORT DOCUMENTATION PAGE

Form Approved
OMB No. 0704-0188

1. REPORT DATE *(DD-MM-YYYY)*	**2. REPORT TYPE**	**3. DATES COVERED** *(From - To)*
January 2019	Technical Report/Final	

4. TITLE AND SUBTITLE

Microstructural Characterization of Snow Compaction Related to Snow Pavements

5a. CONTRACT NUMBER

5b. GRANT NUMBER

5c. PROGRAM ELEMENT NUMBER

6. AUTHOR(S)

Zoe R. Courville, Ross M. Lieblappen, Terry D. Melendy, and Andrew P. Bernier

5d. PROJECT NUMBER

5e. TASK NUMBER
EP-ANT-16-34

5f. WORK UNIT NUMBER

7. PERFORMING ORGANIZATION NAME(S) AND ADDRESS(ES)

U.S. Army Engineer Research and Development Center (ERDC)
Cold Regions Research and Engineering Laboratory (CRREL)
72 Lyme Road
Hanover, NH 03755-1290

8. PERFORMING ORGANIZATION REPORT NUMBER

ERDC/CRREL TR-19-1

9. SPONSORING / MONITORING AGENCY NAME(S) AND ADDRESS(ES)

National Science Foundation, Office of Polar Programs
2415 Eisenhower Avenue
Alexandria, VA 22314

10. SPONSOR/MONITOR'S ACRONYM(S)
NSF

11. SPONSOR/MONITOR'S REPORT NUMBER(S)

12. DISTRIBUTION / AVAILABILITY STATEMENT

Approved for public release; distribution is unlimited.

13. SUPPLEMENTARY NOTES

Engineering for Polar Operations, Logistics, and Research (EPOLAR)

14. ABSTRACT

A first-of-its-kind snow runway for wheeled aircraft operation at McMurdo Station, Antarctica, demonstrated that robust structures can be made of snow that push the limit of what is known about snow strength and how to parameterize it. We conducted a series of laboratory tests to determine the links between snow density and snow compressive strength for very high-density snow structures. We constructed snow samples of varying densities to mimic the snow structures of the constructed runway and measured the resulting snow microstructural and mechanical properties. The goal of this work is to ultimately increase our understanding of the role of density, as an easy-to-measure parameter, in determining snow strength as it relates to snow construction applications (e.g., snow runways, tunnels, and foundations) and how to best quantify the relationships between microstructure, density, and strength of very dense snow structures. Our values for the mechanical properties compared relatively well with the compilation of past historical results. Based on our results, to a first order approximation, snow microstructure data can be used to help improve snow strength predictions. Important future work would focus on improving these snow microstructure-strength relationships to include the effects of meteorological forcing.

15. SUBJECT TERMS

EPOLAR, McMurdo Station (Antarctica), NSF, Snow, Snow--Microstructure, Snow compressive strength, Snow mechanics, Snow pavement, Snow runways, Snow yield strength, Young's modulus

16. SECURITY CLASSIFICATION OF:			**17. LIMITATION OF ABSTRACT**	**18. NUMBER OF PAGES**	**19a. NAME OF RESPONSIBLE PERSON**
a. REPORT	**b. ABSTRACT**	**c. THIS PAGE**			**19b. TELEPHONE NUMBER** *(include area code)*
Unclassified	Unclassified	Unclassified	SAR	43	